

Cite this: *J. Mater. Chem. C*, 2023,  
11, 8052

## Mn<sup>2+</sup>-doped Cs<sub>2</sub>ZnBr<sub>4</sub> scintillator for X-ray imaging†

Binbin Su,<sup>a</sup> Kai Han<sup>a</sup> and Zhiguo Xia<sup>id</sup>\*<sup>ab</sup>

Luminescent metal halides with a high photoluminescence quantum yield (PLQY), large Stokes shift and strong X-ray absorption capability have demonstrated prospects in high-energy radiation detection. Here, we report Mn<sup>2+</sup>-doped all-inorganic metal halide Cs<sub>2</sub>ZnBr<sub>4</sub> as an X-ray imaging scintillator. The as-prepared Cs<sub>2</sub>ZnBr<sub>4</sub>:Mn<sup>2+</sup> shows two emission bands peaking at 526 and 655 nm, respectively, with a PLQY of up to 58.8%. It is found that the dual emissions belong to the spin-forbidden d–d transition of Mn<sup>2+</sup> ions in different coordination configurations, and the involved luminescence and evolution mechanisms have been analyzed. To investigate the scintillation properties, we successfully fabricated a homogeneous thin film scintillation screen containing Cs<sub>2</sub>ZnBr<sub>4</sub>:25%Mn<sup>2+</sup>, which shows good X-ray scintillation performance with a light yield of about 15 600 photons per MeV and a low detection limit of 1.16 μGy<sub>air</sub> s<sup>-1</sup>. Moreover, the flexible and large-area scintillation screens exhibit good X-ray imaging performance with a spatial resolution of 5.06 lp mm<sup>-1</sup> and excellent stability under continuous X-ray irradiation.

Received 6th October 2022,  
Accepted 9th November 2022

DOI: 10.1039/d2tc04249e

rsc.li/materials-c

### 10th Anniversary Statement

Luminescent materials are regarded as crucial elements for advanced optoelectronic devices. Our group has always worked in the field of rare earth phosphors and published two papers on Na<sub>3</sub>(Y,Sc)Si<sub>3</sub>O<sub>9</sub>:Eu<sup>2+</sup> (*J. Mater. Chem. C*, 2013, 1, 5917–5924) and NaBaScSi<sub>2</sub>O<sub>7</sub>:Eu<sup>2+</sup> (*J. Mater. Chem. C*, 2013, 1, 7139–7147) in the first issue of *Journal of Materials Chemistry C*. From 2016, our group began some pioneering work on the luminescent metal halides from doped halide perovskite nanocrystals to versatile metal halide crystals and published their earlier work on Cs(Pb<sub>x</sub>Mn<sub>1-x</sub>)(Cl<sub>y</sub>Br<sub>1-y</sub>)<sub>3</sub> nanocrystals in 2017 (*J. Mater. Chem. C*, 2017, 5, 9281–9287). As a young journal on materials for optical, magnetic and electronic devices, *Journal of Materials Chemistry C* has witnessed the rapid progress of inorganic luminescent materials and also the continual advance and achievement of our group. In 2022, I was appointed as the Associate Editor of *Journal of Materials Chemistry C* and I will have more opportunities to serve for this journal. I am also very glad to publish our recent manuscript on the Mn<sup>2+</sup>-doped Cs<sub>2</sub>ZnBr<sub>4</sub> scintillator for X-ray imaging (*J. Mater. Chem. C*, 2023, 10, DOI: 10.1039/D2TC04249E) in this 10th anniversary themed issue for the *Journal of Materials Chemistry C*. Thanks!

## 1. Introduction

Zero-dimensional (0D) metal halides, as a new type of luminescent materials, have recently attracted much attention due to their low-cost and facile solution-processability.<sup>1–4</sup> In terms of the 0D framework, miscellaneous metal halide anion

sublattices (*e.g.*, tetrahedral BX<sub>4</sub>, pyramidal BX<sub>5</sub>, and octahedral BX<sub>6</sub>, *etc.*) have been adopted,<sup>5–7</sup> and the structural diversity endows them with versatile crystal structures and tunable photophysical properties, which make them promising candidates for potential optoelectronic applications, such as light-emitting diodes (LED), photodetectors, irradiation detectors, and so on.<sup>8–14</sup> In particular, the strong X-ray absorption capability and various crystalline forms (*e.g.*, polycrystalline films, single crystals, and nanocrystals) make 0D metal halides suitable for high-energy radiation detection, which is of great significance in medical diagnosis, industrial flaw detection, *etc.*<sup>15–20</sup>

X-ray imaging technology is mainly based on the penetrativity of X-ray and the difference in the density and thickness between different tissues (*i.e.*, the attenuation difference of X-rays after penetrating different subjects).<sup>21,22</sup> There are generally two main detection mechanisms: direct conversion

<sup>a</sup> The State Key Laboratory of Luminescent Materials and Devices, Guangdong Provincial Key Laboratory of Fiber Laser Materials and Applied Techniques, Guangdong Engineering Technology Research and Development Center of Special Optical Fiber Materials and Devices, School of Materials Science and Engineering, South China University of Technology, Guangzhou 510641, China.

E-mail: xiazg@scut.edu.cn

<sup>b</sup> School of Physics and Optoelectronics, South China University of Technology, Guangzhou 510641, China

† Electronic supplementary information (ESI) available. See DOI: <https://doi.org/10.1039/d2tc04249e>

of X-ray photons into electrical signals in detectors (*i.e.*, direct conversion strategy) and indirect conversion into low energy photons in scintillators (*i.e.*, indirect conversion strategy).<sup>23,24</sup> Conventional semiconductor materials (*e.g.*, Si, CdTe, and CdZnTe) are generally used for direct conversion detection. However, there exist some problems, such as low X-ray blocking capability of Si, and the large noise and nonuniform charge transport of CdTe and CdZnTe due to the charge carrier trapping limit.<sup>25–27</sup> Moreover, complicated preparation processes and expensive preparation cost hinder their further applications. Traditional inorganic scintillators, such as CsI:TI, CdWO<sub>4</sub>, Bi<sub>4</sub>Ge<sub>3</sub>O<sub>12</sub> (BGO), and (Lu,Y)<sub>2</sub>SiO<sub>5</sub> (LYSO) have been successfully applied in indirect conversion X-ray detection due to their low detection limit and high energy resolution, but the inherent shortcomings, such as the complex preparation process, high synthesis temperature and vacuum conditions are also the restricting factors for X-ray imaging applications.<sup>28,29</sup>

Alternatively, the emerging 0D metal halides possess high photoluminescence quantum yields (PLQYs), large Stokes shift (*i.e.*, negligible self-absorption) and strong X-ray absorption capability making them appropriate for indirect conversion X-ray detection.<sup>10,12,15,30,31</sup> As a consequence, it is necessary to discover new luminescent 0D metal halides with good scintillation properties for X-ray imaging. One can then find many reports on the 0D metal halides, which show excellent radioluminescence (RL) properties. Typically, Cs<sub>3</sub>Cu<sub>2</sub>I<sub>5</sub> nanocrystals show strong RL under X-ray irradiation with an extremely high light yield of above 79 279 photons per MeV.<sup>32</sup> Moreover, the X-ray imaging resolution based on the In-doped Cs<sub>3</sub>Cu<sub>2</sub>I<sub>5</sub> single crystals even reaches 18 lp mm<sup>-1</sup>, which is higher than that of the commercial CsI:TI based flat-panel X-ray detectors.<sup>33</sup> Some 0D hybrid metal halide scintillators have also been reported, such as Sn(II)-based Bmpip<sub>2</sub>SnBr<sub>4</sub>,<sup>15</sup> Cu(I)-based (DIET)<sub>3</sub>Cu<sub>3</sub>X<sub>3</sub>,<sup>30</sup> and Mn(II)-based (C<sub>38</sub>H<sub>34</sub>P<sub>2</sub>)MnBr<sub>4</sub>.<sup>17</sup> As a typical example, our group reported the textured TPP<sub>2</sub>MnBr<sub>4</sub> transparent ceramic by seed-crystal-induced cold sintering, which shows a light yield of about 78 000 ± 2000 photons per MeV, a low detection limit of 8.8 nGy<sub>air</sub> s<sup>-1</sup>, and a high spatial resolution of 15.7 lp mm<sup>-1</sup> for X-ray imaging.<sup>11</sup> Besides, our group reported the large size transparent medium based on the 0D hybrid manganese bromide, which also demonstrates good scintillation performances with a low detection limit of 103 nGy<sub>air</sub> s<sup>-1</sup> and a spatial resolution of 13.4 lp mm<sup>-1</sup> for X-ray imaging.<sup>34</sup> However, long-term stability is an index for evaluating the practical application. Although some eco-friendly Sn(II)-, Cu(I)-, and Mn(II)-based 0D hybrid metal halide scintillators show competitive scintillation performances in indirect conversion X-ray detection, their poor stability restricts their development. Therefore, it is urgent to explore 0D metal halide scintillators with good stability for confirming the practical application requirements.

Herein, we reported new Mn<sup>2+</sup>-doped all-inorganic metal halide Cs<sub>2</sub>ZnBr<sub>4</sub> prepared by a facile solution process at room temperature (RT). Under UV excitation, Mn<sup>2+</sup>-doped Cs<sub>2</sub>ZnBr<sub>4</sub> polycrystalline powders show bright yellow-green emission with two peaks at 526 and 655 nm, as well as a PLQY of up to 58.8%. Experimental analysis demonstrates that the observed dual

emissions come from the spin-forbidden d–d transition of Mn<sup>2+</sup> ions in different coordination configurations. Moreover, Cs<sub>2</sub>ZnBr<sub>4</sub>:Mn<sup>2+</sup> shows excellent air and thermal stability, and we fabricated a homogeneous thin film scintillation screen based on Cs<sub>2</sub>ZnBr<sub>4</sub>:25%Mn<sup>2+</sup>, which shows good X-ray scintillation performance with a light yield of about 15600 photons per MeV. The detection limit of 1.16 μGy<sub>air</sub> s<sup>-1</sup> is approximately lower than the dosage for a standard medical diagnosis, moreover, the flexible, large-area scintillation screen exhibits good X-ray imaging performance with a spatial resolution of 5.06 lp mm<sup>-1</sup> and excellent stability under continuous X-ray irradiation.

## 2 Experimental section

### 2.1 Materials

All reagents and solvents were used without further purification, including CsBr (99.9%, Aladdin), ZnBr<sub>2</sub> (99.9%, Aladdin), MnBr<sub>2</sub> (99.5%, Aladdin), HBr aqueous solution (48% in water by weight, Aladdin), ethanol (99.5, Aladdin) and polydimethylsiloxane (PDMS, Sylgard<sup>TM</sup> 182).

### 2.2 Synthesis of undoped and Mn<sup>2+</sup>-doped Cs<sub>2</sub>ZnBr<sub>4</sub> polycrystalline powders

5 mmol CsBr (2.128 g) and 2.5 mol ZnBr<sub>2</sub> (0.563 g) were dissolved in 10 mL HBr aqueous solution to form a clear solution. Then, the prepared solution was filtered using a polyvinylidene fluoride (PVDF) filter with 0.45 μm pore-size to remove unreacted impurities. The filtrate was allowed to cool naturally to RT, the polycrystalline powders were separated out and repeatedly washed using ethanol. Finally, the obtained powders were dried in an oven at 60 °C for 6 h. For Mn<sup>2+</sup>-doped Cs<sub>2</sub>ZnBr<sub>4</sub> polycrystalline powders (Cs<sub>2</sub>Zn<sub>1-x</sub>Mn<sub>x</sub>Br<sub>4</sub>, x = 5%, 10%, 15%, 20%, 25%, 30%), the same method was used, and different proportions of MnBr<sub>2</sub> were added to replace ZnBr<sub>2</sub>.

### 2.3 Synthesis of Cs<sub>2</sub>ZnBr<sub>4</sub>:Mn<sup>2+</sup>-PDMS films

Mn<sup>2+</sup>-doped Cs<sub>2</sub>ZnBr<sub>4</sub> polycrystalline powders were fully ground in an agate mortar for obtaining uniform size distribution. PDMS was prepared by mixing the pre-polymer and curing agent at a volume ratio of 10:1. 25%Mn<sup>2+</sup>-doped Cs<sub>2</sub>ZnBr<sub>4</sub> polycrystalline powders were used to synthesize PDMS films. 2.5 g Cs<sub>2</sub>ZnBr<sub>4</sub>:25%Mn<sup>2+</sup> polycrystalline powders were dispersed in 5 ml ethanol. Subsequently, adding the dispersed powders to 10 g PDMS under sonication to obtain uniform slurry. Finally, the Mn<sup>2+</sup>-doped Cs<sub>2</sub>ZnBr<sub>4</sub>-PDMS thin film can be obtained by a spin coating method, followed by solidifying at 120 °C for 2 h. The thickness of the film can be controlled by speed of the spin coating.

### 2.4 Characterization

The powder X-ray diffraction (PXRD) measurement was performed on an Aeris powder X-ray diffraction (XRD) diffractometer (PANalytical Corporation, Netherlands) operating at 40 kV and 15 mA with a monochromatized Cu K $\alpha$  radiation ( $\lambda = 1.5406 \text{ \AA}$ ) and a linear VANTEC detector. The Rietveld refinements were performed

by using Fullprof. The diffraction pattern was scanned over the angular range of 5–120 degrees ( $2\theta$ ) with a step size of 0.02, at RT. The temperature-dependent PXRD were measured by the same Aeris PXRD diffractometer equipped with BTS 500-benchtop heating stages (PANalytical Corporation, Netherlands). The X-ray photoelectron spectra (XPS) were recorded with a Thermo ESCALAB 250 XI instrument using monochromatic Al K $\alpha$  radiation ( $h\nu = 1486.6$  eV). Inductively coupled plasma optical emission spectroscopy (ICP-OES) was performed on Agilent 720ES. The Fourier transform infrared spectrum (FTIR) was performed on a PerkinElmer Spectrum GX. The photoluminescence (PL) and PL excitation (PLE) spectra at RT were recorded on an FLS1000 fluorescence spectrophotometer (Edinburgh Instruments Ltd, UK) equipped with a continuous xenon lamp (450 W) as an excitation source. The temperature-dependent PL spectra were measured by the same spectrophotometer equipped with Cryo-77 low temperature fluorescence instrument (Tian Jin Orient-KOJI instrument Co., Ltd). The luminescence thermal quenching behavior of the samples was measured by the same spectrophotometer equipped with a TAP-02 high-temperature fluorescence instrument (Tian Jin Orient-KOJI instrument Co., Ltd). The photoluminescence quantum yield (PLQY) was recorded by an integrated sphere, which was attached to the FLS1000 spectrofluorometer. The PLQY was calculated using the following equation:  $\eta_{\text{QY}} = I_{\text{S}}/(E_{\text{R}} - E_{\text{S}})$ , in which  $I_{\text{S}}$  represents the luminescence emission spectrum of the sample,  $E_{\text{R}}$  is the spectrum of the excitation light from the empty integrated sphere (without the sample), and  $E_{\text{S}}$  is the excitation spectrum for the excited sample. Time-resolved emission data were collected at RT using the FLS1000 spectrofluorometer using a microsecond light sources. Time-resolved emission data were collected at RT using the FLS1000 spectrofluorometer. The dynamics of emission decay were monitored by using the FLS1000's time-correlated single-photon counting capability (1024 channels; 2000  $\mu\text{s}$  window) with data collection for 10 000 counts.

**Measurement of radioluminescence (RL) spectra and intensity.** FLS1000 spectrofluorometer (Edinburgh Instruments Ltd, UK) equipped with a X-ray tube (Amptek Inc, Mini-X, Mo target and tube voltage was 50 kV) and an integrating sphere is used to measure the RL spectra. The corresponding RL intensity can be calculated by integrating the RL spectra.

**Calculation of X-ray attenuation efficiency.** The X-ray attenuation efficiency (AE) is calculated by the following formula:

$$\text{AE} = [1 - \exp(-(\mu/\rho)x)] \times 100\%, \quad (1)$$

where  $\mu/\rho$  is the photon cross section function obtained from the XCOM database of National Institute of Standards and Technology (NIST),  $x$  is mass thickness, which is defined as the mass per unit area, and is obtained by multiplying the thickness  $t$  by the density  $\rho$ , *i.e.*,  $x = \rho t$ . Here, we use the approximate density of  $\text{Cs}_2\text{ZnBr}_4$ ,  $3.74 \text{ g cm}^{-3}$ , to calculate attenuation efficiency, moreover, we used 22 keV as the photon energy to calculate the attenuation efficiency *versus* thickness of scintillator.

**Calculation of light yield.** The commercial LuAG:Ce scintillator with a light yield 25 000 photons per MeV is used as a

reference to calibrate the light yield of the  $\text{Cs}_2\text{ZnBr}_4:\text{Mn}^{2+}$  scintillator.  $\text{Cs}_2\text{ZnBr}_4:\text{Mn}^{2+}$  and LuAG:Ce scintillators are set at the same position to measure the RL spectra. Then the corresponding photon counting results were obtained by integrating these RL spectra. Light yield is defined as the ratio of photon numbers emitted from the luminescent sites to the total absorbed X-ray energy, it represents an internal X-ray conversion efficiency. The different scintillators have the different X-ray absorptions even they have the same thickness. Therefore, the emission photon counts of scintillators should be normalized to same X-ray attenuation (100%) as the following formula:<sup>35</sup>

$$\text{PC}_{\text{normalized}} = \frac{\text{PC}_{\text{measured}}}{\text{AE}} \quad (2)$$

where AE is the X-ray attenuation efficiency (%) of scintillators at a certain thickness. The light yield of  $\text{Cs}_2\text{ZnBr}_4:\text{Mn}^{2+}$  scintillators ( $\text{LY}_{\text{sample}}$ ) is calculated by the following formula:

$$\text{LY}_{\text{Sample}} = \text{LY}_{\text{LuAG:Ce}} \frac{\text{PC}_{\text{normalized}}(\text{sample})}{\text{PC}_{\text{normalized}}(\text{LuAG:Ce})} \quad (3)$$

where  $\text{LY}_{\text{LuAG:Ce}}$  is the light yield of LuAG:Ce (25 000 photons per MeV),  $\text{PC}_{\text{normalized}}(\text{sample})$  and  $\text{PC}_{\text{normalized}}(\text{LuAG:Ce})$  are the photon counts of  $\text{Cs}_2\text{ZnBr}_4:\text{Mn}^{2+}$  and commercial LuAG:Ce scintillator normalized to respective X-ray attenuation efficiencies.

**Calculation of the modulation transfer function (MTF).** MTF is defined as the transfer capability of the input signal modulation of spatial frequency, which generally acts as the evaluation index of the spatial resolution performance of the imaging system.  $\text{MTF} = \text{output contrast of the image}/\text{enter the contrast of the image}$ . Since the contrast of the output image is always smaller than that of the input image, thus, the MTF value is between 0 and 1. When the MTF value decreases to 0.2, the spatial resolution can be determined by the corresponding spatial frequency. Here, we adopt the slanted-edge method to calculate the MTF curve. We take an X-ray image using a thin slice of lead (Pb) with sharp edge, the edge spread function (ESF) can be obtained from the slanted-edge profile of this X-ray image. The MTF is calculated by the following equation:<sup>36</sup>

$$\text{MTF}(\nu) = F[\text{LSF}(x)] = F\left(\frac{\text{dESF}(x)}{\text{d}x}\right) \quad (4)$$

where  $\nu$  is the spatial frequency and  $x$  is the position of pixels, and the line spread function (LSF) is the derivative of ESF and the MTF is the Fourier transform of LSF. MTF operation on images can be obtained using software Image J.

## 3 Results and discussion

### 3.1 Structural characterizations of $\text{Mn}^{2+}$ -doped $\text{Cs}_2\text{ZnBr}_4$

All-inorganic  $\text{Cs}_2\text{ZnX}_4$  ( $X = \text{Cl}, \text{Br}$ ) crystallize in orthorhombic space group  $Pnma$ .<sup>37,38</sup> Among them,  $\text{Cs}_2\text{ZnBr}_4$  belongs to a typical 0D structure (Fig. 1(a)), in which  $\text{Zn}^{2+}$  ions are coordinated with four  $\text{Br}^-$  ions forming  $[\text{ZnBr}_4]^{2-}$  tetrahedrons, and the isolated  $[\text{ZnBr}_4]^{2-}$  are separated by the surrounding  $\text{Cs}^+$  cations. A similar ionic radius of  $\text{Zn}^{2+}$  ( $r = 0.60 \text{ \AA}$ , CN = 4) and  $\text{Mn}^{2+}$  ( $r = 0.66 \text{ \AA}$ , CN = 4) along with the tetrahedral coordination

geometries (*i.e.*,  $[\text{ZnBr}_4]^{2-}$  tetrahedrons) make  $\text{Zn}^{2+}$  crystallographic sites more suitable for  $\text{Mn}^{2+}$  doping (Fig. 1(a)).<sup>39–41</sup> The Rietveld refinement of X-ray diffraction (XRD) pattern indicates the high phase purity of  $\text{Mn}^{2+}$ -doped  $\text{Cs}_2\text{ZnBr}_4:\text{Mn}^{2+}$  (Fig. S1, ESI†). Refinement is stable and shows low *R*-factors (Table S1, ESI†). Atom coordinates and main bond lengths of  $\text{Cs}_2\text{ZnBr}_4:\text{Mn}^{2+}$  are shown in Table S2 (ESI†). The peak positions of PXRDs of  $\text{Mn}^{2+}$ -doped  $\text{Cs}_2\text{ZnBr}_4$  polycrystalline powders shift slightly toward low diffraction angles with increased  $\text{Mn}^{2+}$  concentrations (Fig. 1(b)). These results are consistent with the fact that  $\text{Mn}^{2+}$  doping leads to the enlarged unit cells due to the larger ionic radius of  $\text{Mn}^{2+}$  ions than  $\text{Zn}^{2+}$  ions in tetrahedral coordination geometry. For  $\text{Mn}^{2+}$ -doped  $\text{Cs}_2\text{ZnBr}_4$  polycrystalline powders, the actual  $\text{Mn}^{2+}$  concentrations are determined using an inductively coupled plasma optical emission spectrometer (ICP-OES), and the results show that the actual doping of  $\text{Mn}^{2+}$  contents are lower than experimentally expected value (Table S3, ESI†). For the convenience of description, the following discussion will use the experimental expected value to express the doping contents. It is reported that the secondary phase of  $\text{Cs}_2\text{MnBr}_4 \cdot 2\text{H}_2\text{O}$  appears when doping  $\text{Mn}^{2+}$  ions into the  $\text{Cs}_2\text{ZnBr}_4$  matrix.<sup>42</sup> However, we didn't find the existence of the  $\text{Cs}_2\text{MnBr}_4 \cdot 2\text{H}_2\text{O}$  phase in the  $\text{Mn}^{2+}$ -doped  $\text{Cs}_2\text{ZnBr}_4$  matrix by Rietveld refinements (Fig. S1, ESI†). This is owing to the fact that the  $\text{Cs}_2\text{MnBr}_4 \cdot 2\text{H}_2\text{O}$  phase is dependent on the main phase  $\text{Cs}_2\text{ZnBr}_4$  (Fig. S2, ESI†), and the trace secondary phase (*i.e.*,  $\text{Cs}_2\text{MnBr}_4 \cdot 2\text{H}_2\text{O}$ ) cannot be identified by PXRD. To verify the local crystal environments of  $\text{Mn}^{2+}$  in the  $\text{Cs}_2\text{ZnBr}_4$  lattice, the electron paramagnetic resonance (EPR) spectra are measured. Generally, when  $\text{Mn}^{2+}$  ions uniformly distribute in lattice sites, we will observe six well-resolved spectral lines in EPR spectra.<sup>43,44</sup> In our cases, no EPR signal is detected in the pristine  $\text{Cs}_2\text{ZnBr}_4$  sample (Fig. 1(c)), and both in low and high  $\text{Mn}^{2+}$ -doped  $\text{Cs}_2\text{ZnBr}_4$  samples (*e.g.*, 5% and 25%  $\text{Mn}^{2+}$  doping), we only

observe the broadening spectral lines rather than the sextet spectral lines corresponding to  $^{55}\text{Mn}$  nucleus ( $I = 5/2$ ), demonstrating the existence of the secondary phase. Furthermore, we measure the Fourier transform infrared spectrum (FTIR), and the stretching vibration ( $\sim 3438 \text{ cm}^{-1}$ ) of  $-\text{OH}$  group in  $\text{H}_2\text{O}$  molecules (Fig. S3, ESI†) is observed. All of results indicate the existence of the secondary phase (*i.e.*,  $\text{Cs}_2\text{MnBr}_4 \cdot 2\text{H}_2\text{O}$ ) in  $\text{Mn}^{2+}$ -doped  $\text{Cs}_2\text{ZnBr}_4$ . Besides, X-ray photoelectron spectral (XPS) analysis is conducted to identify the valence state of  $\text{Mn}^{2+}$  in  $\text{Cs}_2\text{ZnBr}_4$  matrix (Fig. 1(d)). The Mn core level spectrum shows the Mn  $2p_{3/2}$  peak at 651.5 eV and Mn  $2p_{1/2}$  peak at 654.4 eV with a separation of 2.9 eV, which confirm the existence of the  $\text{Mn}^{2+}$  dopant. In addition, the existence of the minor  $\text{Cs}_2\text{MnBr}_4 \cdot 2\text{H}_2\text{O}$  phase is confirmed by luminescence spectra, which is discussed in below.

### 3.2 Photophysical properties of $\text{Mn}^{2+}$ -doped $\text{Cs}_2\text{ZnBr}_4$ polycrystalline powders

It is previously reported that pristine  $\text{Cs}_2\text{ZnBr}_4$  shows the weak blue emission peaking at 465–470 nm under around 280 nm excitation.<sup>20,45,46</sup> Herein, the normalized photoluminescence (PL) and PL excitation (PLE) spectra of  $\text{Mn}^{2+}$ -doped  $\text{Cs}_2\text{ZnBr}_4$  polycrystalline powders are shown in Fig. 2(a). The PLE spectra contains five peaks located at 296, 365, 379, 441 and 458 nm, which belong to the characteristic transitions of  $\text{Mn}^{2+}$  ions. Under 365 nm excitation,  $\text{Mn}^{2+}$ -doped  $\text{Cs}_2\text{ZnBr}_4$  show the bright yellow-green emission peaking at 526 and 655 nm. For different amounts of  $\text{Mn}^{2+}$  doped  $\text{Cs}_2\text{ZnBr}_4$  samples, the shape and maxima of the PL spectra remain the same (Fig. S4, ESI†). Depending on the increased  $\text{Mn}^{2+}$  concentrations, the PL intensities firstly increase and then decrease due to concentration-quenching, and the sample with the highest PL intensity is obtained when the  $\text{Mn}^{2+}$  concentration reaches 25% (Fig. 2(b)). The PLQYs of different amounts of  $\text{Mn}^{2+}$  doped



**Fig. 1** (a) Crystal structure diagram of  $\text{Cs}_2\text{ZnBr}_4$ , including the proposed  $\text{Mn}^{2+}$  substitution process. (b) Partial PXRD patterns of  $\text{Mn}^{2+}$ -doped  $\text{Cs}_2\text{ZnBr}_4$  samples with different  $\text{Mn}^{2+}$  contents. (c) EPR spectra of undoped and  $\text{Mn}^{2+}$ -doped  $\text{Cs}_2\text{ZnBr}_4$  samples at RT. (d) High-resolution XPS spectrum of Mn 2p for  $\text{Cs}_2\text{ZnBr}_4:25\%\text{Mn}^{2+}$  sample.

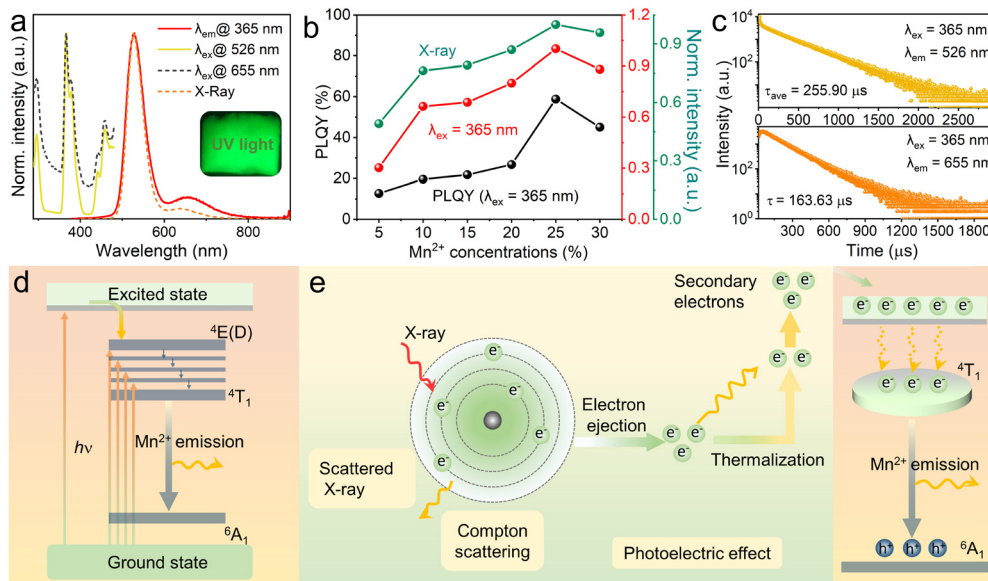


Fig. 2 (a) Normalized PL, PLE and RL spectra of the  $Cs_2ZnBr_4:25\%Mn^{2+}$  sample at RT. (b) PL intensity, RL intensity and the PLQYs of the different  $Mn^{2+}$ -doped  $Cs_2ZnBr_4$  samples. (c) Time-resolved PL spectra of  $Cs_2ZnBr_4:25\%Mn^{2+}$  sample in different excitation and monitoring wavelengths at RT. The proposed PL (d) and RL (e) mechanisms of  $Mn^{2+}$ -doped  $Cs_2ZnBr_4$ .

$Cs_2ZnBr_4$  also show the same variation trend with PL intensities, and the highest PLQY reaches 58.82% when 25%  $Mn^{2+}$  doping (Fig. 2(b) and Table S4, ESI<sup>†</sup>). The PL decay curves of  $Cs_2ZnBr_4:25\%Mn^{2+}$  are determined by time-resolved spectra (Fig. 2(c)), and the red emission band shows the single exponential fitting and green emission band shows the double exponential fitting, and the microsecond level long lifetimes indicated that the dual emissions all come from the spin-forbidden d-d transition ( $4T_1 \rightarrow 6A_1$ ) of  $Mn^{2+}$  ions. The PL lifetimes of different amounts of  $Mn^{2+}$  doped  $Cs_2ZnBr_4$  are shown in Fig. S5 and S6 (ESI<sup>†</sup>). It is found that the PL lifetimes of the green emission band firstly increase and then decrease (Table S5, ESI<sup>†</sup>). However, the PL lifetimes of the red emission bands almost remain unchanged with increased  $Mn^{2+}$  contents (Table S6, ESI<sup>†</sup>).

It is well known that the emission wavelengths of  $Mn^{2+}$  ions are highly dependent on the crystal field surroundings of the host lattices, allowing the characteristic emissions from green to red. Generally,  $Mn^{2+}$  ion in tetrahedral coordination geometry presents the typical green emission with weak ligand field strength and shows the red emission in octahedral coordination geometry with strong ligand field strength.<sup>44</sup> As mentioned above, there is only one type of crystallographic site (*i.e.*, tetrahedral coordination geometry,  $[ZnBr_4]^{2-}$ ) for  $Mn^{2+}$  doping in  $Cs_2ZnBr_4$  matrix, leading to the green emission peaking at 526 nm.

However, the observed red emission band peaking at 655 nm should come from  $Mn^{2+}$  emission with the octahedral coordination geometry. Therefore, by further considering the PXRD analysis, we attribute the red emission to  $Cs_2MnBr_4 \cdot 2H_2O$  phase and dual emission all originate from spin-forbidden d-d transition of  $Mn^{2+}$  ions, which is caused by different coordination configurations of  $Mn^{2+}$  ions. In addition, under X-ray excitation,

$Mn^{2+}$ -doped  $Cs_2ZnBr_4$  shows the bright radioluminescence (RL) with two emission bands, as shown in Fig. 2(a) and Fig. S7 (ESI<sup>†</sup>). Similarly, 25%  $Mn^{2+}$ -doped sample show the strongest RL (Fig. 2(b)). The underlying PL and RL mechanisms for  $Mn^{2+}$ -doped  $Cs_2ZnBr_4$  are depicted in Fig. 2(d) and (e), respectively. Compared with PL mechanism, RL mechanism contains an extra photoelectron conversion process that transfers high-energy electronics to low-energy electronics for radiative recombination.<sup>47</sup> To be precise, firstly, the heavy atoms (*e.g.* Cs, Br, Mn, Zn) of  $Cs_2ZnBr_4:Mn^{2+}$  absorb the radiation energy (*i.e.*, X-ray) mainly by the photoelectric effect and inelastic Compton scattering, ejecting massive hot electrons. Then, the ejected hot electrons are thermalized on an ultrafast timescale and are captured by luminescent centers.

To gain insight into the photophysical properties, temperature-dependent PL spectra of  $Cs_2ZnBr_4:25\%Mn^{2+}$  are measured. Differently, the green emissions are highly dependent on the temperatures, and an obvious blue-shift behavior is observed with the temperatures increase from 80 to 275 K (Fig. 3(a)), due to the enhanced electron-phonon interactions.<sup>48</sup> However, the peak positions of red emissions almost remain unchanged. Similarly, the PL intensities of these two emissions gradually decrease with the increase of temperatures, which is caused by the PL thermal quenching resulting from the thermal dissociation of excitons.<sup>49</sup> We also analyze the PL thermal quenching behavior above room temperature (Fig. 3(b)).

Interestingly, with the temperatures increase from RT to 100 °C, the integrated PL intensities of green emissions show obvious improvement, and the integrated PL intensity at 100 °C even becomes 2.42 times that of the initial PL intensity. When temperatures continually increase from 100 to 250 °C, the integrated PL intensities of green emissions gradually decrease. At 250 °C, the integrated PL intensity of green emission still



**Fig. 3** (a) Temperature-dependent PL spectra of  $\text{Cs}_2\text{ZnBr}_4:25\%\text{Mn}^{2+}$  sample 365 nm upon excitation along with temperature range from 80 to 275 K. (b) Temperature-dependent PL spectra of  $\text{Cs}_2\text{ZnBr}_4:25\%\text{Mn}^{2+}$  sample upon 365 nm excitation along with temperature range from RT to 250 °C. (c) Normalized integrated PL intensities of green and red emissions in  $\text{Cs}_2\text{ZnBr}_4:25\%\text{Mn}^{2+}$  sample at different temperatures. (d) Temperature-dependent *in situ* PXRDs of  $\text{Cs}_2\text{ZnBr}_4:25\%\text{Mn}^{2+}$  sample along with temperature range from RT to 200 °C (e) Schematic illustration for unusual PL thermal enhancement process in  $\text{Mn}^{2+}$ -doped  $\text{Cs}_2\text{ZnBr}_4$  samples.

maintains the 75% of the initial PL intensity (Fig. 3(c)). In addition, the integrated PL intensities of red emissions show the obvious decrease with the increase of temperatures, and when temperatures are higher than 100 °C, the red emissions almost disappeared. Furthermore, Fig. 3(d) shows the temperature-dependent *in situ* PXRD of the  $\text{Cs}_2\text{ZnBr}_4:25\%\text{Mn}^{2+}$  sample, and on account of the heating-induced lattice expand process that enhances the cell volumes, the diffraction peak positions shift slightly toward lower angles. Moreover, when increasing temperatures from RT to 200 °C, the diffraction peak intensities of PXRD gradually increase, demonstrating the gradual removal of the second phase (*i.e.*,  $\text{Cs}_2\text{MnBr}_4\cdot 2\text{H}_2\text{O}$ ) with increasing temperature. This result is consistent with the PL thermal quenching behavior. By combining structural transformation and PL thermal quenching behavior, we propose the underlying thermal quenching mechanism, as shown in Fig. 3(e).  $\text{Cs}_2\text{MnBr}_4\cdot 2\text{H}_2\text{O}$  contains two  $\text{H}_2\text{O}$  molecules, and the  $\text{H}_2\text{O}$  molecules are gradually volatilized and accompanied with the decomposition with increasing temperatures. Then, the extra free  $\text{Mn}^{2+}$  ions generated by the structural decomposition enter the  $\text{Zn}^{2+}$  sites. With the increase of  $\text{Mn}^{2+}$  contents, the PL intensities of the green emission gradually increase, when temperatures reach 100 °C, the  $\text{Cs}_2\text{MnBr}_4\cdot 2\text{H}_2\text{O}$  phase is completely decomposed. Therefore, the PL intensities of green emissions reach the maximum at 100 °C, while the red emissions completely disappeared at 100 °C. With further increasing temperatures from 100 to 250 °C, normal thermal quenching behavior occurs, thus, the PL intensities of green emissions gradually decrease. Benefiting from the high stability of the all-inorganic  $\text{Cs}_2\text{ZnBr}_4$  structure, the PL intensity of the green emission still maintains 75% of the initial PL intensity

even at 250 °C. Soon afterwards, with the decrease of temperature, the samples absorb the moisture in air accompanied with the recovery of  $\text{Cs}_2\text{MnBr}_4\cdot 2\text{H}_2\text{O}$  phase. Finally, the samples recover the original PL behavior, exhibiting the dual emissions. In addition,  $\text{Mn}^{2+}$ -doped  $\text{Cs}_2\text{ZnBr}_4$  polycrystalline powders show the remarkable stability under other conditions, such as continuous UV illumination, and storage under ambient conditions (Fig. S8 and S9, ESI<sup>†</sup>).

### 3.4 Photophysical properties of the $\text{Mn}^{2+}$ -doped $\text{Cs}_2\text{ZnBr}_4$ @PDSM thin film

The low-cost and facile solution synthesis method and good photophysical properties make  $\text{Cs}_2\text{ZnBr}_4:25\%\text{Mn}^{2+}$  polycrystalline powders highly promising as X-ray scintillators in indirect conversion X-ray detection. To investigate the scintillation properties, the homogeneous flexible films were fabricated by a conventional spin-coating method. First, fresh  $\text{Cs}_2\text{ZnBr}_4:25\%\text{Mn}^{2+}$  powders were ground in a mortar for obtaining uniform-sized powders. After mixing  $\text{Cs}_2\text{ZnBr}_4:25\%\text{Mn}^{2+}$  powders with PDMS under ultrasonic conditions, the obtained slurry was dropped and spin-coated on a glass substrate, followed by solidifying at 120 °C for 2 h. The thicknesses of the obtained PDMS thin film screens containing  $\text{Cs}_2\text{ZnBr}_4:25\%\text{Mn}^{2+}$  powders can be controlled by changing the spin speed. Finally, we obtained a uniform, large-sized ( $10 \times 10 \text{ cm}^2$ ), and transparent  $\text{Cs}_2\text{ZnBr}_4:25\%\text{Mn}^{2+}$ @PDSM thin film (Fig. 4(a) and (b)), and this film also shows bright yellow-green emission under UV excitation (Fig. 4(c)). Moreover, this film shows large flexibility, which can be folded, twisted, and stretched (Fig. 4(d)–(f)). In addition, the  $\text{Cs}_2\text{ZnBr}_4:25\%\text{Mn}^{2+}$ @PDSM thin film shows the slightly decreased PLQY of 56.35% compared with  $\text{Cs}_2\text{ZnBr}_4:25\%\text{Mn}^{2+}$  polycrystalline powders (Fig. S9, ESI<sup>†</sup>).



Fig. 4 (a) and (b) Photographs of large-sized and transparent  $\text{Cs}_2\text{ZnBr}_4:25\%\text{Mn}^{2+}$ @PDSM thin film under visible light. (c) Photograph of  $\text{Cs}_2\text{ZnBr}_4:25\%\text{Mn}^{2+}$ @PDSM thin film under 365nm UV light. Photographs of the flexible  $\text{Cs}_2\text{ZnBr}_4:25\%\text{Mn}^{2+}$ @PDSM thin film at different mechanical deformations under UV excitation: folding (d), twisting (e), and stretching (f).

However, the as-prepared thin film shows improved environmental stability, and when exposed to air conditions (30% relative humidity and 30 °C) for about one week, only a 5% reduction of the PLQYs is observed. The improved environmental stability may be caused by the increased hydrophobicity.

Fig. 5(a) shows the X-ray absorption coefficients (steady-state X-ray energy: 22 keV) of the  $\text{Cs}_2\text{ZnBr}_4:25\%\text{Mn}^{2+}$  and the typical commercial scintillators (LuAG:Ce and CsI:TI) in broad range of photon energies based on the photon cross-section database.<sup>35</sup> The absorption of  $\text{Cs}_2\text{ZnBr}_4:25\%\text{Mn}^{2+}$  in the region for medical

digital radiography (*i.e.*, 18–30 keV) is slightly higher than CsI:TI and slightly lower than LuAG:Ce. Fig. 5(b) shows the X-ray attenuation efficiency of  $\text{Cs}_2\text{ZnBr}_4:25\%\text{Mn}^{2+}$  and typical scintillators (LuAG:Ce and CsI:TI) as a function of thickness at a X-ray photon energy of 22 keV.  $\text{Cs}_2\text{ZnBr}_4:25\%\text{Mn}^{2+}$  shows the same X-ray attenuation efficiency with a LuAG:Ce scintillator. The RL spectra of  $\text{Cs}_2\text{ZnBr}_4:25\%\text{Mn}^{2+}$ @PDSM thin film and LuAG:Ce scintillators are measured under the same conditions, as shown in Fig. 5(c). The  $\text{Cs}_2\text{ZnBr}_4:25\%\text{Mn}^{2+}$ @PDSM thin film shows similar PL and RL spectra, indicating that the same radiative

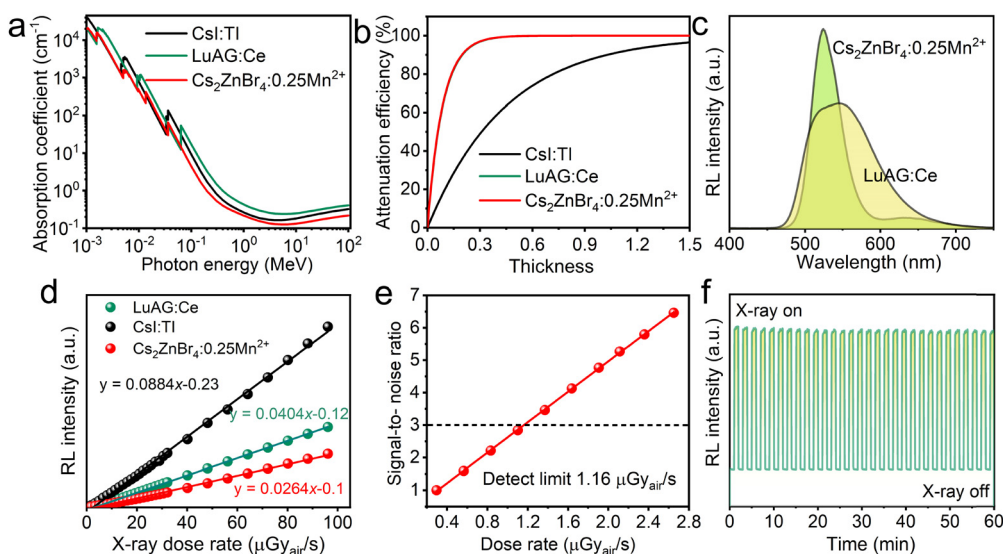


Fig. 5 (a) Absorption coefficients of  $\text{Cs}_2\text{ZnBr}_4:25\%\text{Mn}^{2+}$ , LuAG:Ce and CsI:TI scintillators as a function of photon energy from 1 keV to 100 MeV. (b) Attenuation efficiency of  $\text{Cs}_2\text{ZnBr}_4:25\%\text{Mn}^{2+}$ , LuAG:Ce and CsI:TI scintillators as a function of photon energy of 22 keV. (c) RL spectra of  $\text{Cs}_2\text{ZnBr}_4:25\%\text{Mn}^{2+}$  and LuAG:Ce scintillators (tube voltage: 50 kV; dose rate:  $96.09 \mu\text{Gy}_{\text{air}} \text{s}^{-1}$ ). (d) Normalized integrated RL intensities of  $\text{Cs}_2\text{ZnBr}_4:25\%\text{Mn}^{2+}$ , LuAG:Ce and CsI:TI scintillators as a function of different X-ray dose rates. (e) Linear relationship between signal-to-noise ratio value and X-ray dose rates. (f) Photostability of the  $\text{Cs}_2\text{ZnBr}_4:25\%\text{Mn}^{2+}$  scintillator under cyclical X-ray illumination.

recombination channel appears upon X-ray and UV excitations. Because  $\text{Cs}_2\text{ZnBr}_4\text{:Mn}^{2+}$  has similar X-ray attenuation efficiencies with commercial LuAG:Ce scintillator, we select the thickness value as 0.3 mm for LuAG:Ce and the scintillator in this work to evaluate the response under various X-ray dose rates. As shown in Fig. 5(d), the as-prepared thin film scintillator presents good linearity to the X-ray dose rates in a large range from  $0.45 \mu\text{Gy}_{\text{air}} \text{s}^{-1}$  to  $96.09 \mu\text{Gy}_{\text{air}} \text{s}^{-1}$ , which is beneficial for obtaining good imaging contrast. Light yield is one of the important indicators for evaluating the performance of scintillators, which can be indirectly obtained from the linear response curves. The response of the  $\text{Cs}_2\text{ZnBr}_4\text{:25\%Mn}^{2+}\text{@PDSM}$  thin film is 0.624 times that of the commercial LuAG:Ce scintillator, and we could obtain the light yield of  $\sim 15\,600$  photons per MeV. Then, the  $\text{Cs}_2\text{ZnBr}_4\text{:25\%Mn}^{2+}\text{@PDSM}$  thin film was used as a reference to determine the light yield of the well-known CsI:Tl scintillator under the same conditions. The light yield of the CsI:Tl scintillator was calculated to be  $\sim 54\,100$  photons per MeV, which is close to its reported value (54 000 photons per MeV). We compare the RL properties of the  $\text{Cs}_2\text{ZnBr}_4\text{:25\%Mn}^{2+}\text{@PDSM}$  thin film with recently reported metal halide scintillators (Table S7, ESI<sup>†</sup>), and the light yield of our sample is close to that of the  $\text{Rb}_2\text{CuCl}_3$  scintillator reported recently.<sup>50</sup> The lowest detection limit is also an important indicator for determining the minimum dose rate required for detection. It can be defined under the dose rate at which the signal to noise ratio (SNR) equals 3.<sup>11</sup> Fig. 5(e) shows the linearity of RL intensity as a function of low dose rate for the  $\text{Cs}_2\text{ZnBr}_4\text{:25\%Mn}^{2+}\text{@PDSM}$  thin film scintillation screen, and the lowest detection limit is determined to be about  $1.16 \mu\text{Gy}_{\text{air}} \text{s}^{-1}$ , which is lower than the dose rate of  $5.5 \mu\text{Gy}_{\text{air}} \text{s}^{-1}$  required for X-ray medical diagnostics.<sup>35</sup> In addition, our scintillator shows the good stability, when exploring

X-ray illumination, the RL intensities of our thin film scintillation screen only show the minor fluctuations (Fig. 5(f)).

### 3.5 X-ray imaging based on the $\text{Cs}_2\text{ZnBr}_4\text{@PDSM}$ thin film scintillation screen

To prove the practicability of our thin film scintillation screen in X-ray imaging, we have employed our homemade X-ray imaging optical system (Fig. S10, ESI<sup>†</sup>). The first target object used is an aluminum specimen box containing a metal spring inside, as shown in Fig. 6(a), and the spring can normally not be observed in visible light. However, when exposing to X-ray illumination, contrast images are obtained, which show a clear metal spring inside (Fig. 6(b) and (c)). To further demonstrate the X-ray imaging capability, we use a ball-point pen and a metallic key partially wrapped in rubber as target objects, this  $\text{Cs}_2\text{ZnBr}_4\text{:25\%Mn}^{2+}\text{@PDSM}$  thin film scintillation screen also exhibits clear images of the inside structure (Fig. 6(d)–(f)). To characterize the spatial resolution of X-ray imaging, the modulation transfer function (MTF) of the image is obtained by the slanted-edge method. As shown in Fig. 6(g), a spatial resolution of  $5.06 \text{ lp mm}^{-1}$  can be achieved when the MTF is 0.2, which is comparable with the recently reported scintillator  $\text{Cs}_2\text{Ag}_{0.6}\text{Na}_{0.4}\text{In}_{0.85}\text{Bi}_{0.15}\text{Cl}_6$  (4.4), and  $\text{CsMnCl}_3\text{:1\%Pb}$  (4.3) scintillators.<sup>47,51</sup> All of the results demonstrate the potential of the  $\text{Cs}_2\text{ZnBr}_4\text{:25\%Mn}^{2+}\text{@PDSM}$  thin film scintillation screen in nondestructive image detection applications.

## 4 Conclusions

In conclusion,  $\text{Mn}^{2+}$ -doped  $\text{Cs}_2\text{ZnBr}_4$  luminescent metal halides and their composite film are reported in this work, and the crystals show unusual dual emissions peaking at 526

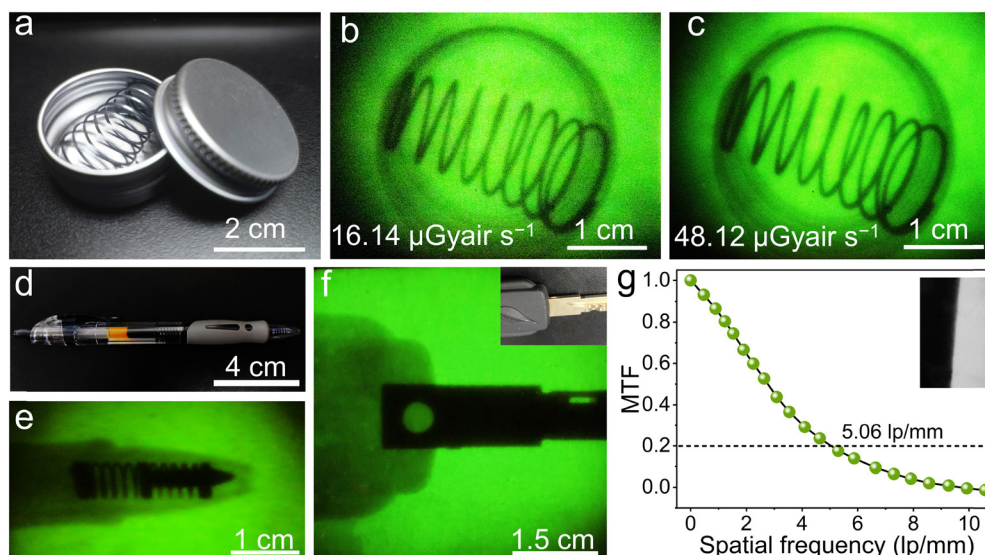


**Fig. 6** (a) Photograph of aluminum specimen box with an iron spring under visible light. (b) and (c) X-ray imaging of an aluminum specimen box with an iron spring under the X-ray doses of  $16.14$  and  $48.12 \mu\text{Gy}_{\text{air}} \text{s}^{-1}$ , respectively. (d) Photograph of the ball-point pen. (e) X-ray imaging of the ball-point pen under the X-ray dose of  $16.14 \mu\text{Gy}_{\text{air}} \text{s}^{-1}$ . (f) X-ray imaging of a metallic key partially wrapped in rubber under the X-ray dose of  $16.14 \mu\text{Gy}_{\text{air}} \text{s}^{-1}$ , inset shows the photograph of the same metallic key. (g) MTF of the  $\text{Cs}_2\text{ZnBr}_4\text{:25\%Mn}^{2+}$  thin film scintillation screen measured by the slanted-edge method (inset).



and 655 nm with the highest PLQY of 58.8% when 25%Mn<sup>2+</sup> doping. PL studies demonstrate that the dual emissions come from the spin-forbidden d–d transition of Mn<sup>2+</sup> ions located at different coordination configurations in different doped matrices, Cs<sub>2</sub>ZnBr<sub>4</sub> and Cs<sub>2</sub>MnBr<sub>4</sub>·2H<sub>2</sub>O phases. In addition, Mn<sup>2+</sup>-doped Cs<sub>2</sub>ZnBr<sub>4</sub> show good stabilities. For demonstrating the potential as an X-ray scintillator, a homogeneous flexible thin film scintillation screen based on Cs<sub>2</sub>ZnBr<sub>4</sub>:25%Mn<sup>2+</sup>@PDSM is fabricated, which shows improved environmental stability and good X-ray scintillation performance, including a modest light yield of 15 600 photons per MeV and a low detection limit of 1.16 μGy<sub>air</sub> s<sup>-1</sup>. Moreover, the clear X-ray images of the target objects were observed by using such a film screen, and the spatial resolution could reach 5.06 lp mm<sup>-1</sup>, demonstrating potential in X-ray imaging.

## Conflicts of interest

The authors declare no conflicts of interest.

## Acknowledgements

This work was supported by the National Natural Science Foundation of China (No. 51961145101), the State Key Laboratory of Luminescent Materials and Devices (Skllmd-2022-02) and the Local Innovative and Research Teams Project of Guangdong Pearl River Talents Program (2017BT01X137).

## Notes and references

- M. Z. Li and Z. G. Xia, *Chem. Soc. Rev.*, 2021, **50**, 2626–2662.
- O. F. Mohammed, *J. Phys. Chem. Lett.*, 2019, **10**, 5886–5888.
- C. K. Zhou, L. J. Xu, S. Lee, H. R. Lin and B. W. Ma, *Adv. Opt. Mater.*, 2020, **9**, 2001766.
- L. Zhou, J. F. Liao and D. B. Kuang, *Adv. Opt. Mater.*, 2021, **9**, 2100544.
- A. Vogler and H. Nikol, *Comments Inorg. Chem.*, 1993, **14**, 245–261.
- H. Nikol, A. Becht and A. Vogler, *Inorg. Chem.*, 2002, **31**, 3277–3279.
- L. Zhou, J. F. Liao, Z. G. Huang, J. H. Wei, X. D. Wang, H. Y. Chen and D. B. Kuang, *Angew. Chem., Int. Ed.*, 2019, **58**, 15435–15440.
- G. J. Zhou, B. B. Su, J. L. Huang, Q. Y. Zhang and Z. G. Xia, *Mater. Sci. Eng., R*, 2020, **141**, 100548.
- J. Kundu and D. K. Das, *Eur. J. Inorg. Chem.*, 2021, 4508–4520.
- Q. Q. He, C. K. Zhou, L. J. Xu, S. J. Lee, X. S. Lin, J. Neu, M. Worku, M. Chaaban and B. W. Ma, *ACS Mater. Lett.*, 2020, **2**, 633–638.
- K. Han, K. Sakhatskiy, J. Jin, Q. Zhang, M. V. Kovalenko and Z. Xia, *Adv. Mater.*, 2022, **34**, e2110420.
- J. H. Wei, Y. W. Yu, J. B. Luo, Z. Z. Zhang and D. B. Kuang, *Adv. Opt. Mater.*, 2022, **10**, 2200724.
- Y. C. Liu, Z. Xu, Z. Yang, Y. X. Zhang, J. Cui, Y. H. He, H. C. Ye, K. Zhao, H. M. Su, R. Lu, M. Liu, M. G. Kanatzidis and S. Liu, *Matter*, 2020, **3**, 180–196.
- B. B. Su, M. Z. Li, E. H. Song and Z. G. Xia, *Adv. Funct. Mater.*, 2021, **31**, 2105316.
- V. Morad, Y. Shynkarenko, S. Yakunin, A. Brumberg, R. D. Schaller and M. V. Kovalenko, *J. Am. Chem. Soc.*, 2019, **141**, 9764–9768.
- X. M. Li, J. X. Chen, D. D. Yang, X. Chen, D. L. Geng, L. F. Jiang, Y. Wu, C. F. Meng and H. B. Zeng, *Nat. Commun.*, 2021, **12**, 3879.
- L. J. Xu, X. S. Lin, Q. Q. He, M. Worku and B. W. Ma, *Nat. Commun.*, 2020, **11**, 4329.
- C. W. E. van Eijk, *Phys. Med. Biol.*, 2002, **47**, R85–R106.
- H. Li, Y. Zhang, M. Zhou, H. Y. Ding, L. Zhao, T. M. Jiang, H. Y. Yang, F. Zhao, W. Q. Chen, Z. W. Teng, J. B. Qiu, X. Yu, Y. M. Yang and X. H. Xu, *ACS Energy Lett.*, 2022, **7**, 2876–2883.
- Y. C. Zhou, Q. Zhou, X. W. Niu, Z. G. Yan, T. F. Lin, J. W. Xiao and X. D. Han, *Inorg. Chem. Front.*, 2022, **9**, 2987–2996.
- T. Y. He, Y. Zhou, X. J. Wang, J. Yin, L. Gutiérrez-Arzaluz, J. X. Wang, Y. H. Zhang, O. M. Bakr and O. F. Mohammed, *ACS Energy Lett.*, 2022, **7**, 2753–2760.
- Y. Zhou, J. Chen, O. M. Bakr and O. F. Mohammed, *ACS Energy Lett.*, 2021, **6**, 739–768.
- J. T. Cao, Z. Guo, S. Zhu, Y. Fu, H. Zhang, Q. Wang and Z. J. Gu, *ACS Appl. Mater. Interfaces*, 2020, **12**, 19797–19804.
- T. T. Xu, Y. Y. Li, M. Nikl, R. Kucerkova, Z. Y. Zhou, J. Chen, Y. Y. Sun, G. D. Niu, J. Tang, Q. Wang, G. H. Ren and Y. T. Wu, *ACS Appl. Mater. Interfaces*, 2022, **14**, 14157–14164.
- Z. W. Pan, L. Wu, J. Z. Jiang, L. Shen and K. Yao, *J. Phys. Chem. Lett.*, 2022, **13**, 2851–2861.
- H. T. Wei, Y. J. Fang, P. Mulligan, W. Chirazzi, H. H. Fang, C. C. Wang, B. R. Ecker, Y. L. Gao, M. A. Loi, L. Cao and J. S. Huang, *Nat. Photonics*, 2016, **10**, 333–339.
- L. Gao and Q. F. Yan, *Sol. RRL*, 2019, **4**, 1900210.
- W. J. Li, L. L. Liu, M. R. Tan, Y. H. He, C. J. Guo, H. M. Zhang, H. T. Wei and B. Yang, *Adv. Funct. Mater.*, 2021, **31**, 2107843.
- L. Lu, M. Z. Sun, Q. Y. Lu, T. Wu and B. L. Huang, *Nano Energy*, 2021, **79**, 105437.
- K. Han, J. C. Jin, B. B. Su, J. W. Qiao and Z. G. Xia, *Adv. Opt. Mater.*, 2022, **10**, 2200865.
- L. Y. Lian, X. Wang, P. Zhang, J. S. Zhu, X. W. Zhang, J. B. Gao, S. Wang, G. J. Liang, D. L. Zhang, L. Gao, H. S. Song, R. Chen, X. Z. Lan, W. X. Liang, G. D. Niu, J. Tang and J. B. Zhang, *J. Phys. Chem. Lett.*, 2021, **12**, 6919–6926.
- L. Y. Lian, M. Y. Zheng, W. Z. Zhang, L. X. Yin, X. Y. Du, P. Zhang, X. W. Zhang, J. B. Gao, D. L. Zhang, L. Gao, G. D. Niu, H. S. Song, R. Chen, X. Z. Lan, J. Tang and J. B. Zhang, *Adv. Sci.*, 2020, **7**, 2000195.
- Q. Wang, Q. Zhou, M. Nikl, J. W. Xiao, R. Kucerkova, A. Beitlerova, V. Babin, P. Prusa, V. Linhart, J. K. Wang, X. M. Wen, G. D. Niu, J. Tang, G. H. Ren and Y. T. Wu, *Adv. Opt. Mater.*, 2022, **10**, 2200304.

- 34 B. H. Li, Y. Xu, X. L. Zhang, K. Han, J. C. Jin and Z. G. Xia, *Adv. Opt. Mater.*, 2022, **10**, 2102793.
- 35 T. M. Jiang, W. B. Ma, H. Zhang, Y. Tian, G. Lin, W. G. Xiao, X. Yu, J. B. Qiu, X. H. Xu, Y. Yang and D. X. Ju, *Adv. Funct. Mater.*, 2021, **31**, 2009973.
- 36 Q. S. Chen, J. Wu, X. Y. Ou, B. L. Huang, J. Almutlaq, A. A. Zhumekeenov, X. W. Guan, S. Y. Han, L. L. Liang, Z. G. Yi, J. Li, X. J. Xie, Y. Wang, Y. Li, D. Y. Fan, D. B. L. Teh, A. H. All, O. F. Mohammed, O. M. Bakr, T. Wu, M. Bettinelli, H. H. Yang, W. Huang and X. G. Liu, *Nature*, 2018, **561**, 88–93.
- 37 B. Morosin and E. C. Lingafelter, *Acta Crystallogr.*, 1959, **12**, 744–745.
- 38 R. Puget, M. Jannin, R. Perret, L. Godefroy and G. Godefroy, *Ferroelectrics*, 1990, **107**, 229–234.
- 39 B. B. Su, M. S. Molokeev and Z. G. Xia, *J. Mater. Chem. C*, 2019, **7**, 11220–11226.
- 40 G. J. Zhou, Z. Y. Liu, J. L. Huang, M. S. Molokeev, Z. W. Xiao, C. G. Ma and Z. G. Xia, *J. Phys. Chem. Lett.*, 2020, **11**, 5956–5962.
- 41 V. Morad, I. Cherniukh, L. Pottschacher, Y. Shynkarenko, S. Yakunin and M. V. Kovalenko, *Chem. Mater.*, 2019, **31**, 10161–10169.
- 42 J. Almutlaq, *Engineering of Lead-Free Materials for Light-Emitting Application: Structural and Photophysical Studies*, 2020.
- 43 B. B. Su, M. S. Molokeev and Z. G. Xia, *J. Phys. Chem. Lett.*, 2020, **11**, 2510–2517.
- 44 B. B. Su, G. J. Zhou, J. L. Huang, E. H. Song, A. Nag and Z. G. Xia, *Laser Photonics Rev.*, 2021, **15**, 2000334.
- 45 P. F. Cheng, L. Feng, Y. F. Liu, D. Y. Zheng, Y. B. Sang, W. Y. Zhao, Y. Yang, S. Q. Yang, D. H. Wei, G. X. Wang and K. L. Han, *Angew. Chem., Int. Ed.*, 2020, **59**, 21414–21418.
- 46 M. Wang, R. T. Yang, S. S. Cheng, G. Q. Li, M. C. Jia, X. Chen, D. Wu, X. J. Li and Z. F. Shi, *J. Phys.: Condens. Matter*, 2022, **34**, 204009.
- 47 W. J. Zhu, W. B. Ma, Y. R. Su, Z. Chen, X. Y. Chen, Y. G. Ma, L. Z. Bai, W. G. Xiao, T. Y. Liu, H. M. Zhu, X. F. Liu, H. F. Liu, X. Liu and Y. M. Yang, *Light: Sci. Appl.*, 2020, **9**, 112.
- 48 R. S. Zeng, K. Bai, Q. L. Wei, T. Chang, J. Yan, B. Ke, J. L. Huang, L. S. Wang, W. C. Zhou, S. Cao, J. L. Zhao and B. S. Zou, *Nano Res.*, 2021, **14**, 1551–1558.
- 49 G. Blasse, *J. Chem. Phys.*, 1969, **51**, 3529–3530.
- 50 X. Zhao, G. D. Niu, J. S. Zhu, B. Yang, J. H. Yuan, S. R. Li, W. R. Gao, Q. S. Hu, L. X. Yin, K. H. Xue, E. Lifshitz, X. S. Miao and J. Tang, *J. Phys. Chem. Lett.*, 2020, **11**, 1873–1880.
- 51 L. Q. Guan, S. Shi, X. W. Niu, S. C. Guo, J. Zhao, T. M. Ji, H. Dong, F. Y. Jia, J. W. Xiao, L. D. Sun and C. H. Yan, *Adv. Sci.*, 2022, **9**, e2201354.